Journal of Biomedical Optics

SPIEDigitalLibrary.org/jbo

Quantitative evaluation of degenerated tendon model using combined optical coherence elastography and acoustic radiation force method

Guangying Guan
Chunhui Li
Yuting Ling
Ying Yang
Jan B. Vorstius
Robert P. Keatch
Ruikang K. Wang
Zhihong Huang

SPIE

Quantitative evaluation of degenerated tendon model using combined optical coherence elastography and acoustic radiation force method

Guangying Guan,[a,b*] Chunhui Li,[a,b*] Yuting Ling,[a] Ying Yang,[c] Jan B. Vorstius,[a] Robert P. Keatch,[a] Ruikang K. Wang,[b] and Zhihong Huang[a]
[a]University of Dundee, School of Engineering, Physics and Mathematics, Dundee DD14HN, Scotland, United Kingdom
[b]University of Washington, Department of Bioengineering, 3720 15th Ave NE, Seattle, Washington 98195
[c]Keele University, Institute for Science and Technology in Medicine, School of Medicine, Stoke-on-Trent ST4 7QB, United Kingdom

Abstract. Damage of collagen fibers in tendons is often directly related to changes in a tendon's mechanical properties. Direct quantitative elasticity measurement of tendons will provide important information in tendon dysfunction diagnosis and treatment assessment. A feasibility study of quantifying the mechanical properties of a degenerated tendon model by a nondestructive imaging modality, which combines optical coherence elastography and acoustic radiation force (ARF) method, is presented. The degenerated tendon model was produced by the partial degradation of chicken tendons through incubation with collagenase at different concentrations and incubation times. A 30-kHz longitudinal ultrasound transducer was used to provide an ARF signal, which was detected by an ultra-high sensitive phase sensitive optical coherence tomography (PhS-OCT) system. The experimental results demonstrate that the combination of ARF method and PhS-OCT can measure the elasticity of tendon quantitatively. The corresponding changes in tendon elasticity due to the application of collagenase have been revealed by this new imaging modality. This method can potentially be used in the assessment of tissue engineering products and in the diagnosis and treatment progression of tendon diseases. [DOI: 10.1117/1.JBO.18.11.111417]

Keywords: acoustic radiation force; phase sensitive optical coherence tomography; optical coherence elastography; tendon elastic properties.

Paper 130282SSRR received Apr. 25, 2013; revised manuscript received Aug. 23, 2013; accepted for publication Sep. 4, 2013; published online Nov. 5, 2013.

1 Introduction

Tendons are composed of uniaxial orientated collagen fibril bundles in hydrated elastin and proteoglycans matrix.[1–5] Its role is to reduce the impedance mismatch of the different tissues when transmitting contractile forces from the muscle to the skeleton[1,2,5] at the osseotendenous junction. Physical trauma in tendons due to high rate loading, laceration, or degeneration due to ageing will rupture/damage collagen fibers, which will cause changes in tendon mechanical behavior.[6,7] Thus, the measurement of the mechanical properties of tendons is of great importance, e.g., in predicting the severity of the injury to the tendons involved;[8] for diagnosis of tendon diseases;[9] in monitoring treatment procedures, e.g., tendon surgical repair;[10,11] or for quantitative evaluation of tendon construction in tendon tissue engineering.[12]

A number of techniques have been developed for evaluation of the tendon mechanical properties, especially the Young's modulus of tendon tissue.[13,14] Extensive studies on isolated animal or human tendon material have been done under quasi-static loading conditions, which undergo elongation to failure.[13–15] However, these methods are destructive. Recently, non-destructive imaging techniques became increasingly popular to investigate muscle and tendon function, including magnetic resonance imaging (MRI) and real time ultrasonography and the corresponding elastography technique using strain or shear wave methods.[16,17] These modalities offer *in vivo* measurement of muscle-tendon morphology and mechanical properties. However, the spatial resolutions of these techniques are limited by the resolution of ultrasound or MRI, which is a scale of tens to hundreds of micron scale. This limits their application in the musculoskeletal system and for characterization of early-phase tendon disease diagnosis and treatment.

Optical coherence elastography (OCE)[18–26] has several advantages over other imaging modalities. It is a noninvasive imaging technique with ultra-high resolution, which is at least an order higher than ultrasound or MRI elastography. It is capable of providing ultra-high microstructural and mechanical characterization of human soft tissues, and therefore has promising clinical applications. This technique monitors the passive tissue responses of the samples stimulated by speckle[19–23] and the Doppler signals.[24–26] Phase sensitive optical coherence tomography (PhS-OCT) combined with shear or surface acoustic wave (SAW) methods have become increasingly popular in tissue characterization. Liang and Boppart used PhS-OCT to measure the shaker induced continuous surface wave *in vivo* on human skin. This method was able to quantify the bulk elastic properties of skin tissues.[27] Li et al.[28–30] introduced SAW by external shaker or Q-switch laser pulse on sample surface. Using this method, bulk quantitative elasticity

*These authors contributed equally to this work.

Address all correspondence to: Zhihong Huang, University of Dundee, School of Engineering, Physics and Mathematics, Dundee DD14HN, Scotland, United Kingdom. Tel: +44 (0)1382 385477; Fax; +44 (0)1382 385508; E-mail: z.y.huang@dundee.ac.uk

information of different layers of phantom and *in vivo* human skin has been estimated. Kennedy et al.[31] applied OCE for *in vivo* characterization of normal and hydrated human skins, relying on the dynamic OCT system in combination with a designed ring actuator, which induces longitudinal vibration to samples. More recently, this technique was developed in providing the three-dimensional OCE images of human skin.[32] However, they do not provide a quantitative measurement of elasticity in these studies. Furthermore, there has been no report for measurements on tendon tissues using the OCT-based elastography modality.

This paper thus explores the use of OCE to provide localized and quantitative mechanical properties of tendons. To achieve this goal, we applied a modulated acoustic radiation force (ARF) to chicken tendons *ex vivo* to induce phase change caused by the vibration. The tendon samples are treated with collagenase to mimic degenerated tissues and then imbedded into 2% agar-agar phantom. A PhS-OCT was utilized to record the phase change of the agar phantom as well as the *ex vivo* tendon, from which the quantitative Young's modulus was deduced.

2 Materials and Methods

2.1 *System Configuration*

The system consists of both the generation of longitudinal waves (induced by an in-house designed and fabricated 30-kHz ultrasound transducer) and detection by PhS-OCT for soft tissue. The setup is schematically shown in Fig. 1.

In order to generate acoustic signals for the elasticity measurement, a transducer with resonant frequency of 30 kHz, which was driven by a square-wave modulated radiation force (RF) signal (50% duty cycle amplifier modulation), was used. The modulation frequency was set to 30 kHz, and the maximum actuator displacement applied to the sample was ~50 nm to ensure the generated strain was in the pure linear-elastic regime. In all experiments, samples were directly placed on the ultrasound transducer. The ARF could then be transmitted from the transducer to compress the samples and trigger vibration in the axial direction.

Detection of the vibration signal was performed using a PhS-OCT system, which has been described in detail previously.[31,32]

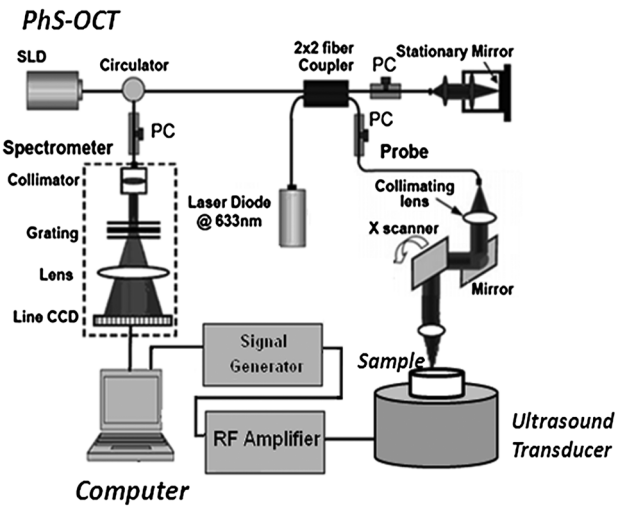

Fig. 1 System set up of ARF combining spectral-domain PhS-OCT system for tendon elasticity evaluation.

Briefly, the PhS-OCT system employed a superluminescent diode as a light source, with a center wavelength of ~1310 nm and a bandwidth of ~83 nm, implemented by a spectral domain configuration. The sample arm used an objective lens of ~50-mm focal length to deliver the detection light on the sample that coupled the vibration signals into the PhS-OCT for detection. The system provided an axial resolution of 8.9 μm and a transverse resolution of 18 μm in air. The acquisition rate was determined by the spectrometer employed in the system that had a maximum rate of ~92,000 A-scans/s. For signal detection, the system was configured as M-mode acquisition while the OCT probe beam stayed constantly in one location of the sample. The system provided a phase sensitivity to the sample displacement of ~200 pm when working in M-scan mode. Two thousand and forty-eight A-scans were acquired to obtain one frame of M-mode scan which takes about 22.3 ms. The structural image of the samples generated by the PhS-OCT system is shown as a function of depth.

2.2 *Sample Preparation*

To prove the accuracy of the ARF method, three double layer phantoms with ~2% agar over ~1% agar, ~3% agar over ~2% agar and ~3% agar over ~1% agar and with ~1 mm of upper layer thickness were created for testing.

To investigate the effectiveness of the OCE system in the detection of degenerative changes in tendinopathy, collagenase from Clostridium histolyticum (type collagen, Sigma, China) was used to degrade the collagen in the tendon to form a degenerated tendon model similar to pathological diseases. The collagenase powder was dissolved in deionised water to different concentrations. Tendons dissected from fresh nonfrozen chicken (bought from supermarket) were treated with different collagenase concentrations (1 mg/mL, 3.3 mg/mL, and 10 mg/mL) and with different incubation times (0, 30, 60, and 90 min) in the incubator at 37°C and 5% CO_2. The collagenase was removed from the tendons in order to stop further digestion after the defined culture time.

After the treatments, tendons were imbedded in 2% agar-agar with ~0.5 to 1 mm thickness from the agar phantom surface. Agar is known to have very low scattering properties; thus, milk was added to each phantom at a concentration of 1% to produce a scattering background similar to what is found in biological tissues. Agar also keeps the tendon hydrated. For each concentration and incubation time span, five samples were prepared for experiment.

3 Data Acquisition and Processing

The application of ARF generates vibration within the sample, which can be observed and detected as phase shift on PhS-OCT. We calculated the phase difference between the first and all the other A-lines ($\phi_i - \phi_1$), where i is a value between 1 and 2048 and ϕ is the phase angle of the A-line at a specific depth. It has been observed that the phase changed at each depth in Fig. 2(a) as dark and light bands through time. These bands represent a frequency response at 30 kHz, as shown in Fig 2(c), which is the modulation of the ultrasound transducer.

Figure 2(b) shows the phase differences, i.e., vibration through time at a depth of 700 μm from the sample surface [the depth location was identified with an arrow in Fig. 2(a)]. Vibration amplitude, which is directly related to the strain, was highly sensitive to the change of material elasticity. Under the same stress, softer material has higher strain and

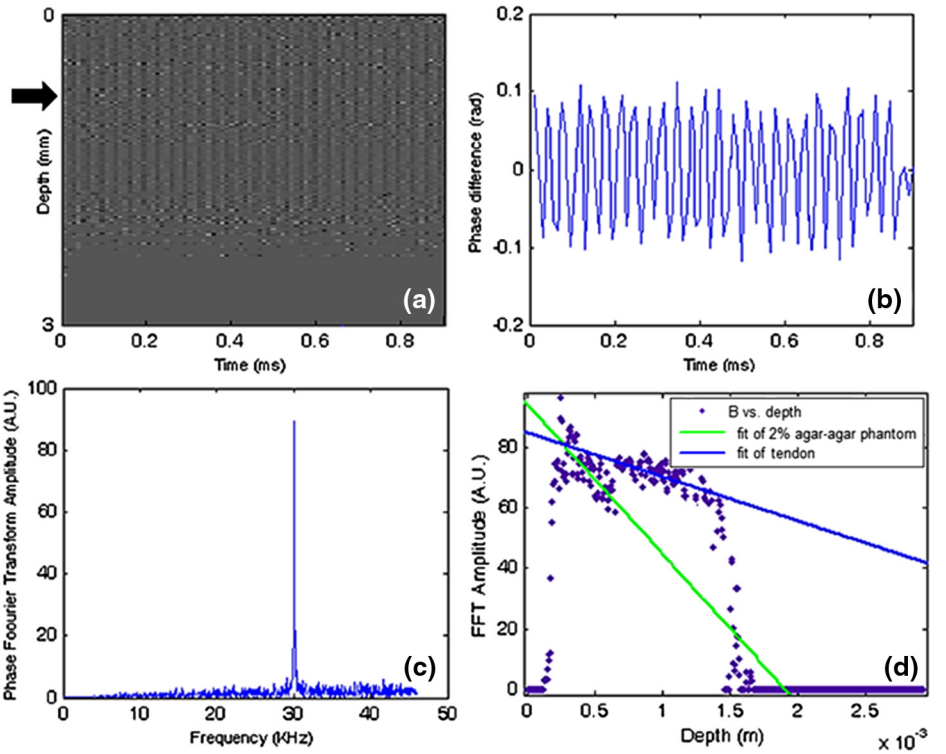

Fig. 2 (a) M-scan of the phase difference obtained from the tendon-agar sample. (b) Phase difference as a function of time at a depth of ~700 μm below the tissue surface [arrow in (a)]. (c) Absolute value of the Fourier transform of the phase difference (c). (d) FFT amplitude of the phase at different depths for sample (linear fit of agar layer-green line and tendon layer-blue line).

stiffer material has smaller strain. With respect to the Hooke's law of elasticity, Young's modulus is the ratio of stress to strain within the elastic region, which can be expressed as

$$E = \frac{\sigma}{\varepsilon}, \tag{1}$$

where E is the Young's modulus, σ is stress, and ε is strain. In the application of OCE to a two-layered sample, constant stress fields can be assumed to apply to both layers. Thus, under the same stress ($\sigma_1 \approx \sigma_2$), in a heterogeneous material, the ratio of Young's modulus in different layers 1 and 2 is equal to the inverse ratio of the strain

$$\frac{E_1}{E_2} = \frac{\frac{\sigma_1}{\varepsilon_1}}{\frac{\sigma_2}{\varepsilon_2}} = \frac{\sigma_1 \varepsilon_2}{\sigma_2 \varepsilon_1} \approx \frac{\varepsilon_2}{\varepsilon_1}. \tag{2}$$

Here, the local strain is determined from the detected tissue displacement caused by the vibration amplitude:[31]

$$\varepsilon = \frac{\Delta L}{L} = \frac{d_2 - d_1}{\Delta z}, \tag{3}$$

where d_1 is the displacement amplitude estimated at a depth of z from the top of the sample and d_2 is the displacement amplitude estimate at a depth of $z + \Delta z$.

Figure 2(c) presents the results of fast Fourier transform (FFT) of the phase difference [FFT ($\Delta\phi$)] and therefore, the amplitude from the data shown in Fig 2(b). A peak at 30 kHz is clearly observed. The amplitude of this peak at each depth, after subtracting the background noise and averaging all the A-lines, is used to create the phase FFT amplitude signal as a function of depth [Fig. 2(d)]. The phase difference caused by the vibration and the phase FFT amplitude are linearly related.[33] Combining Eqs. (2) and (3), if we take the Δz to be long enough, the ratio between the slope of FFT amplitude from agar phantom and tendon gives the ratio of strain, i.e., the inverse ratio of Young's modulus.

A linear polynomial model has been chosen to fit the averaged phase FFT amplitude of both 2% agar layer and tendon layer in one sample [Fig. 2(d) green line and blue line] with 95% confidence bounds. The beginning and ending point of the fitting is decided by the surface of the agar and the interface of the two layers, however, we need to sacrifice some fitting length due to the inaccuracy of data, which may be caused by some noise at the surface or sharp attenuation of backscattering light intensity at the deep part. Then, the slopes of the linear fit can be determined. Taking previous measurement values of the Young's modulus for 2% agar-agar phantom, 193 kPa,[29] and using the above mentioned inversion method, the quantitative Young's modulus of tendon can be evaluated.

4 Results and Discussion

Figure 3 shows the amplitude of the FFT of the phase changes caused by the ARF at different depths in both ~2% agar over ~1% agar and ~3% agar over ~2% agar phantoms. From Eqs. (2) and (3), if we make the Δz long enough to cover the whole layer thickness, the ratio of slope of the FFT amplitude from different layers of the sample is equal to the ratio of shear wave strain. Thus, we apply a linear polynomial model fitted to the averaged phase FFT amplitude of different layers of phantoms (Fig. 3, blue line and red dash line) with 95% confidence bounds. From Figs. 3(a) and 3(b), we find that at higher agar concentration, the slope of FFT amplitude curve is smaller, as under the same stress the stiffer material will have a smaller strain.

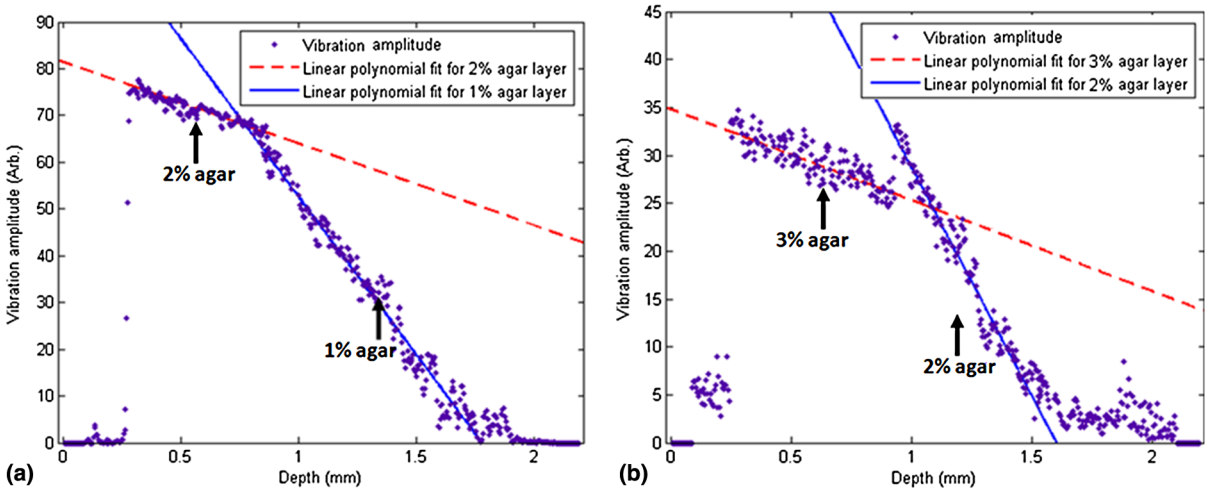

Fig. 3 FFT amplitude of the phase changes caused by the shear wave amplitude at different depths and the linear model fit of (a) ~2% agar over ~1% agar and (b) ~3% agar over ~2% agar phantoms.

From our previous study, the average phase velocities calculated from SAW signals were $\sim 12.33 \pm 1.03$ m/s, $\sim 7.55 \pm 1.09$ m/s, and $\sim 4.87 \pm 0.94$ m/s which yields a Young's modulus of $\sim 515 \pm 3.59$ kPa, $\sim 193 \pm 4.01$ kPa, and $\sim 80 \pm 2.99$ kPa for the 3%, 2%, and 1% phantoms, respectively.[29] In Fig. 3(a), the estimated slopes of FFT amplitude curves for 1% agar layer and 2% agar layer are −67.51 and −25.57, respectively. The slope ratio of 2% and 1% is 2.64, which approximates the inverse ratio of Young's modulus of the two concentrations (2.41 = 193 kPa/80 kPa). Similarly in Fig. 3(b), the estimated slope of FFT amplitude curves for 2% agar layer and 3% agar layer is −122.19 and −47.36. The ratio is 2.58, which approximates the inverse ratio of Young's modulus of 3% and 2% agar (2.66 = 515 kPa/193 kPa). We then try the phantom of ~3% agar over ~1% agar, which shows a more significant difference in Young's modulus (results shown in Fig. 4). As expected, the slope ratio of 1% agar and 3% agar vibration amplitude is 6.64 (−109.6/ − 16.5), which is similar to the inverse ration of Young's modulus of 3% and 1% agar (6.43 = 515 kPa/80 kPa).

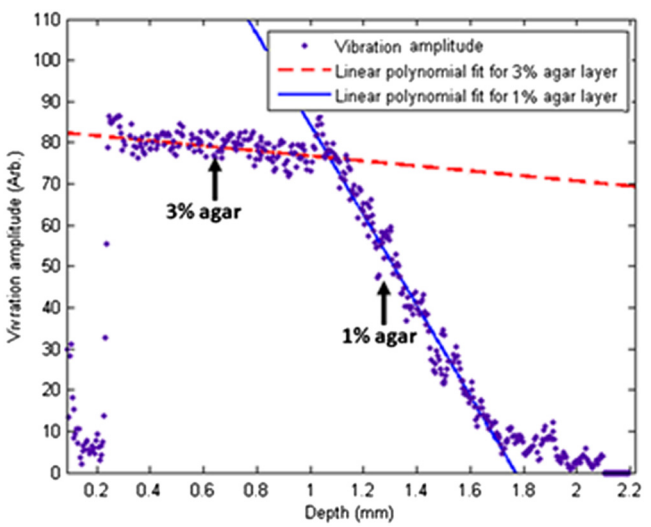

Fig. 4 FFT amplitude of the phase changes caused by the shear wave amplitude at different depths and the linear model fit of ~3% agar over ~1% agar.

From the above phantom experiments, we have proven that the strain ratio, which is equal to the ratio of FFT vibration amplitude curve slopes, is approximate to the inverse ratio of its corresponded Young's modulus. Knowing the ratio and Young's modulus of any one material, the quantitative elasticity of connected other materials can be calculated easily.

There is an amplitude increase at the boundary between stiffer material and softer material, as seen in Figs. 3(b) and Fig. 4. This is due to the fact that the shear wave travels from stiffer material to softer material and so the transmitted wave amplitude will be greater than the incident shear wave. The percentage is dependent on the materials' acoustic impedances, which is the result of material density and acoustic wave velocity:

$$\frac{A_t}{A_i} = \frac{2z_1}{z_1 + z_2} = \frac{2\rho_1 c_1}{\rho_1 c_1 + \rho_2 c_2}, \tag{4}$$

where A_t (A_i) is the transmitted (incident) wave amplitude, and z, ρ, and c are the acoustics impedance, density, and the acoustic wave velocity of the material. A stiffer material has higher density and shear wave velocity, thus, phenomena of amplitude increase can be observed.

Figure 5(a) shows the real-time cross-sectional microstructures image (B-scan) of control tendon in a 2% agar phantom captured by the PhS-OCT system. The OCT image clearly demarcates the tendon tissue at ~0.8 mm depth below the phantom surface in this sample. It provides an indicator and cross-validation of the tendon boundary which can be used for the linear fit of the agar and the tendon layers. The vertical dash line indicates the depth range that can be detected by the OCT system. At the depth of 2 mm, the system also stops the phase shift detection. Figure 5(b) shows FFT amplitude of the phase changes caused by the ARF-induced vibration at different depths. Straight lines show linear model fits of the 2% agar area and control tendon without treatment. The estimated FFT amplitude curve slopes for the agar phantom layer and the control tendon are −9.367e + 004 and −1377, respectively. This gives a phantom-tendon slope ratio of 68. We assume that both the agar layer and tendon layer are homogeneous, then this value can be treated as the ratio of strain for

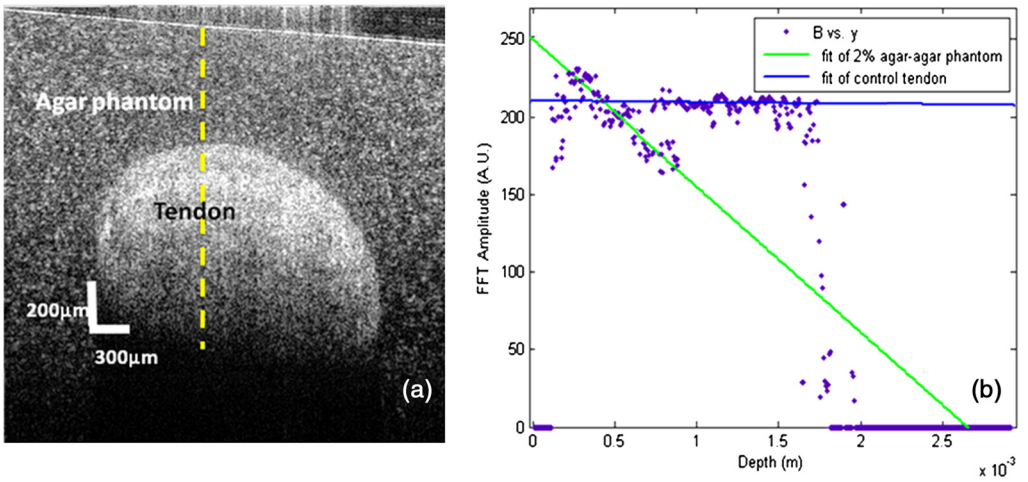

Fig. 5 (a) Typical OCT image of 2% agar-tendon phantom, yellow dash line indicates the position of PhS-OCT detection beam for the phase change. (b) Averaged FFT amplitude of the phase changes caused by ARF-induced vibration at different depths and the linear model fit of (green) ~2% agar (blue) of control tendon.

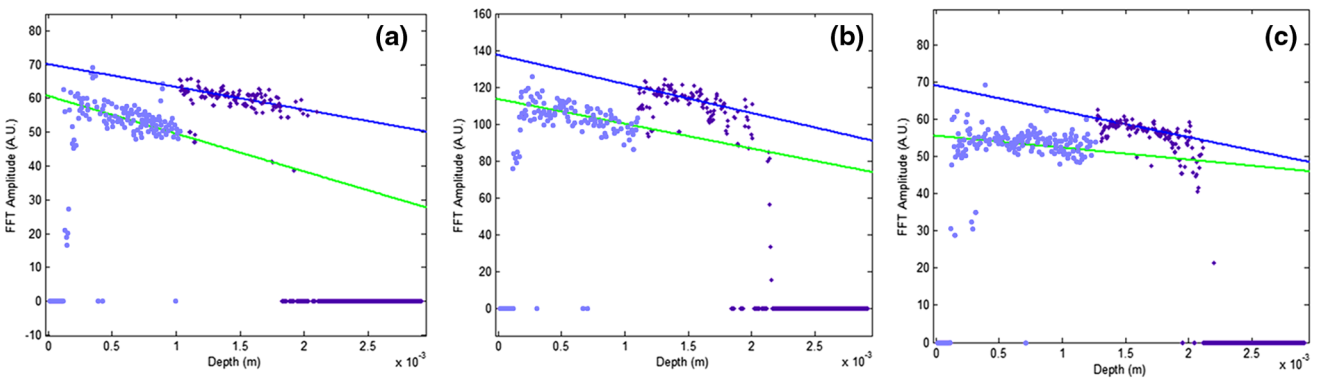

Fig. 6 Typical averaged FFT amplitude of the phase changes caused by ARF-induced vibration at different depths and the linear model fit of ~2% agar (green fit line with slate blue data points) and of treated tendon (blue fit line with purple data points) with collagenase concentration of 10 mg/mL (a) 30 min, (b) 60 min, and (c) 90 min.

these two layers. According to Eq. (2), the Young's modulus of control tendon can be estimated as 13124 kPa (~193 kPa × 68).

Figure 6 shows typical averaged FFT amplitudes and the linear fits of the phase differences caused by ARF-induced vibration as the function of depth of tendon-agar samples that were treated with collagenase solution (10 mg/mL and 30 min). As seen in Fig. 6(a), the slope difference between ~2% agar phantom and tendon sample was greatly reduced compared to the control group in Fig. 5(b). This result indicates the Young's modulus of the tendon sample has been reduced, as was expected because collagen fibers have been damaged by collagenase. With the treatment time increased to 60 and 90 min, the averaged FFT amplitude slopes of tendons became nearly equal to [Fig. 6(b)] and larger [Fig. 6(c)] than that of the agar phantom, which indicates that the Young's modulus was equal and smaller than that of agar phantom with 60 and 90 min treatment, respectively.

Figure 7 shows the overall Young's modulus changes of collagenase treated tendon samples with different incubation times and concentrations, and the quantitative Young's modulus is summarized in Table 1. As expected, the Young's modulus

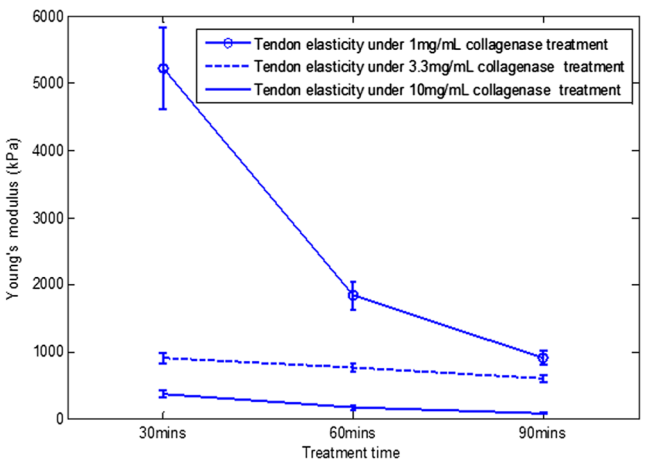

Fig. 7 Overall Young's modulus changes of collagenase-treated tendon samples with different time span and different concentrations.

Table 1 Summary of collagenase treated tendon Young's modulus (kPa).

Control	16750.0 ± 878.1		
Subjecting to collagenase treatment	30 min	60 min	90 min
1 mg/mL	5211.9 ± 610.3	1833.5 ± 199.2	899.4 ± 107.9
3.3 mg/mL	895.2 ± 84.8	724.3 ± 52.1	602.2 ± 55.3
10 mg/mL	366.7 ± 61.0	177.6 ± 37.1	88.4 ± 9.3

of tendon tissue is decreased as a function of collagenase digestion. Higher concentration of collagenase and longer treatment time led to a larger Young's modulus decrease.

Figure 8 shows the OCT structure images, OCE images, and the overlaid images of tendon samples treated with collagenase for 1, 3.3, and 10 mg/mL for 60 min, respectively. The two-dimensional strain image was calculated based on the method developed from our previous study.[33] Applying Eq. (2) and using the Young's modulus value of 193 kPa for the agar phantom, the strain image was converted to the OCT elastography image with absolute Young's modulus values, as shown in Figs. 8(d)–8(f), instead of relative strain value as shown in Kennedy et al.[31] It shows that using the presented elasticity reconstruction approach based on combined ARF and OCE methods, quantitative elasticity images of an agar-tendon sample can be reconstructed with high resolution. A clear

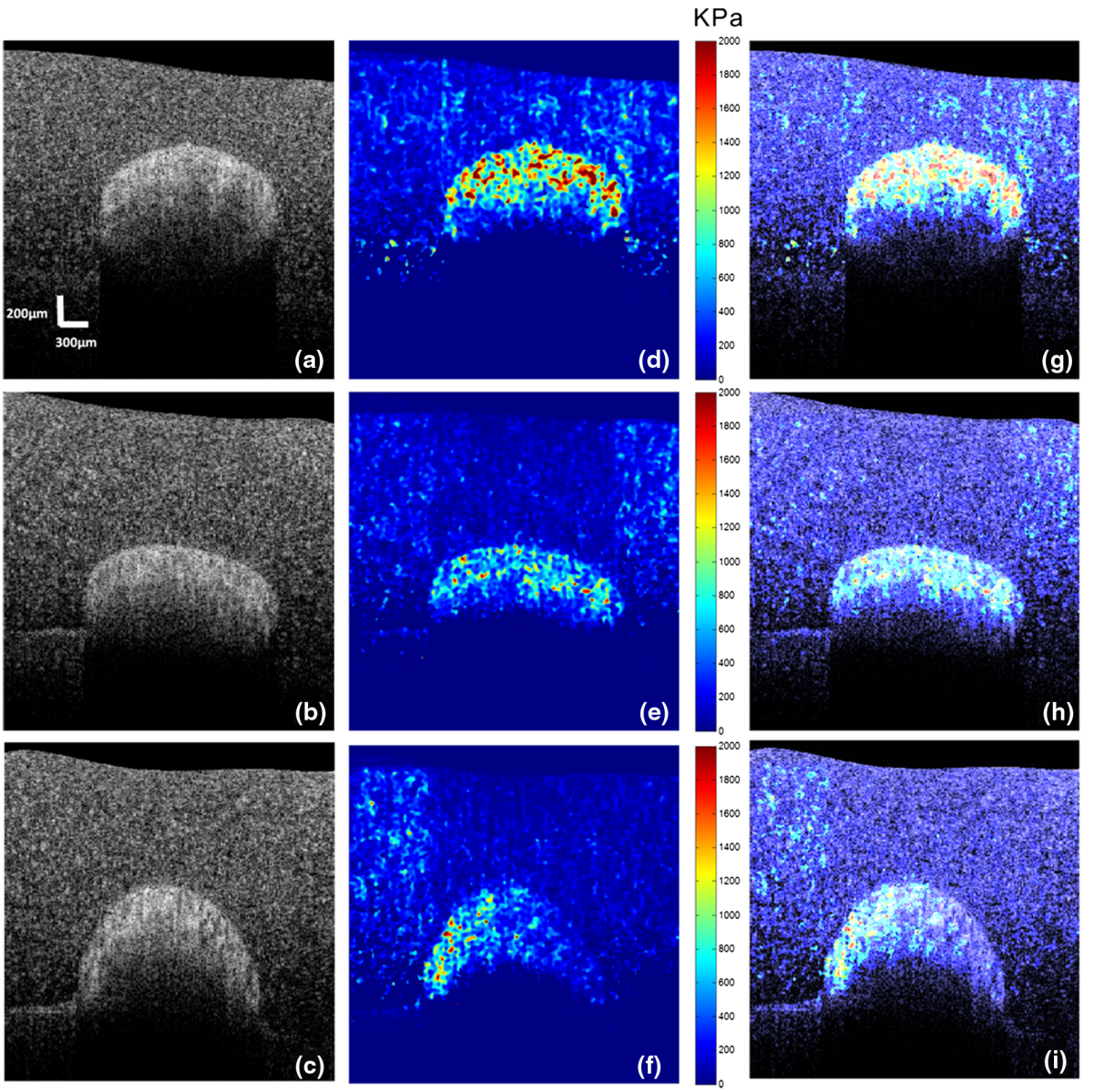

Fig. 8 (a)–(c) are the structure images of tendon samples treated with 1, 3.3, and 10 mg/mL collagenase for 60 min, respectively; (d)–(f) are the calculated Young's modulus elastography for these three samples and the color bars show the value in unit of KPa; (g)–(i) are overlaid images [uneven parts of the tendon elastography in figure (f) could be caused by the treatment].

tendon-agar boundary can be found in the elasticity images although the signal decreases at deeper locations. This is expected because the accuracy of the phase measurement relies on the intensity level from structure image.[33]

5 Conclusions

A novel concept of combining an ARF method and PhS-OCT to characterize and monitor the quantitative information of chicken tendons *ex vivo* is reported in this paper. Experiments show that the method can efficiently monitor the elasticity change of the tendon due to different collagen fiber degradation. PhS-OCT is also an ideal tool to detect the ARF vibration as it provides high signal to noise ratio (SNR) on tendon samples. It is able to provide the B-frame image of the sample, which may validate the thickness estimation in elastography, while providing the elastography of the tendon tissues. The Young's modulus measured from our method corresponded well with the predicted results.

A benefit of PhS-OCT based elastography, in addition to being noninvasive and noncontact, is real-time simultaneous tomographic imaging of the tendon samples. The concept reported in this paper can be developed further into a truly quantitative elastographic imaging system, which has great application value in tissue engineering to evaluate the growth of artificial tendon tissue in real-time as nondisruptive feedback for bioreactors.[34] With further development of the PhS-OCT system, this method may have a great potential in real clinical diagnosis to assess the physiological conditions of human tendons. In future work, this method can be combined with the needle probe OCT. The insertion of an OCT probe into deep tissue will overcome the penetration limits of OCT light beam.

References

1. R. F. Ker, "The implications of the adaptable fatigue quality of tendons for their construction repair and function," *Comp. Biochem. Physiol., Part A, Mol. Integr. Physiol.* **133**(4), 987–1000 (2002).
2. K. G. Vogel, "Breakout session 5: tendon and ligament," *Clin. Orthop.* **367**(Suppl.), S371–S374 (1999).
3. S. L. Woo et al., "Tissue engineering of ligament and tendon healing," *Clin. Orthop.* **367**(Suppl.), S312–S323 (1999).
4. B. D. Fornage, *Ultrasonography of Muscles and Tendons—Examination Technique and Atlas of Normal Anatomy of The Extremities*, pp. 30–37, SpringerVerlag, New York (1989).
5. R. McN. Alexander, "Mechanics of skeleton and tendons," in *Handbook of Physiology, Section A, The Nervous System*, B. Brook, Ed., Vol. 2, pp. 17–42, American Physiological Society, Bethesda (1981).
6. C. T. M. Davies et al., "Adaptation of mechanical properties of muscle to high force training in man," *J. Physiol.* **365**, 277–284 (1985).
7. A. J. Banes and P. Weinhold et al., "Gap junctions regulate responses of tendon cells ex vivo to mechanical loading," *Clin. Orthop.* **367**(Suppl.), S356–S370 (1999).
8. D. L. Butler and H. A. Awad, "Perspectives on cell and collagen composites for tendon repair," *Clin. Orthop.*, **367**(Suppl.), S324–S332 (1999).
9. K. Yasuda and K. Hayashi, "Changes in biomechanical properties of tendons and ligaments from joint disuse," *Osteoarthritis Cartilage* **7**(1), 122–129 (1999).
10. G. T. Kuwada, "An update on repair of Achilles tendon rupture. Acute and delayed," *J. Am. Podiatr. Med. Assoc.* **89**(6), 302–306 (1999).
11. H. Kubota et al., "Effect of motion and tension on injured flexor tendons in chickens," *J. Hand Surg.* **21**(3), 456–463 (1996).
12. F. Goulet et al., "Tendon and ligament," in *Principles of Tissue Engineering*, 2nd ed., R. Lanza, R. Langer, and J. Vacanti, Eds., pp. 711–722, Academic Press, San Diego, CA (2000).
13. M. B. Bennett et al., "Mechanical properties of various mammalian tendons," *J. Zool.* **209**(4), 537–548 (1986).
14. R. L. Lieber et al., "Frog semitendinosis tendon loadstrain and stress-strain properties during passive loading," *Am. J. Physiol.* **261**(1 Pt 1), C86–C92 (1991).
15. J. D. Goldstein et al., "Development of a reconstituted collagen tendon prosthesis. A preliminary implantation study," *J. Bone Jt. Surg. Am.* **71**(8), 1183–1191 (1989).
16. T. Fukunaga et al., "Tendinous movement of a human muscle during voluntary contractions determined by real time ultrasonography," *J. Appl. Physiol.* **81**(3), 1430–1433 (1996).
17. T. Fukunaga et al., "Physiological crosssectional area of human leg muscles based on magnetic resonance imaging," *J. Orthop. Res.* **10**(6), 926–934 (1992).
18. C. Sun, B. Standish, and V. X. D. Yang, "Optical coherence elastography: current status and future applications," *J. Biomed. Opt.* **16**(4), 043001 (2011) .
19. J. M. Schmitt, "OCT elastography: imaging microscopic deformation and strain of tissue," *Opt. Express* **3**(6), 199–211 (1998).
20. R. C. Chan et al., "OCT-based arterial elastography: robust estimation exploiting tissue biomechanics," *Opt. Express* **12**(19), 4558–4572 (2004).
21. J. Rogowska et al., "Optical coherence tomographic elastography technique for measuring deformation and strain of atherosclerotic tissues," *Heart* **90**(5), 556–562 (2004).
22. H. J. Ko et al., "Optical coherence elastography of engineered and developing tissue," *Tissue Eng.* **12**(1), 63–73 (2006).
23. R. K. K. Wang, Z. H. Ma, and S. J. Kirkpatrick, "Tissue Doppler optical coherence elastography for real time strain rate and strain mapping of soft tissue," *Appl. Phys. Lett.* **89**(14), 144103 (2006).
24. S. J. Kirkpatrick, R. K. Wang, and D. D. Duncan, "OCT-based elastography for large and small deformations," *Opt. Express* **14**(24), 11585–11597 (2006).
25. X. Liang et al., "Optical micro-scale mapping of dynamic biomechanical tissue properties," *Opt. Express* **16**(15), 11052–11065 (2008).
26. R. K. Wang, S. Kirkpatrick, and M. Hinds, "Phase-sensitive optical coherence elastography for mapping tissue microstrains in real time," *Appl. Phys. Lett.* **90**(16), 164105 (2007).
27. X. Liang and S. A. Boppart, "Biomechanical properties of in vivo human skin from dynamic optical coherence elastography," *IEEE Trans. Biomed. Eng.* **57**(4), 953–959 (2010).
28. C. H. Li, Z. H. Huang, and R. K. K. Wang, "Elastic properties of soft tissue-mimicking phantoms assessed by combined use of laser ultrasonics and low coherence interferometry," *Opt. Express* **19**(11), 10153–10163 (2011).
29. C. Li et al., "Determining elastic properties of skin by measuring surface waves from an impulse mechanical stimulus using phase-sensitive optical coherence tomography," *J. R. Soc. Interface* **9**(70), 831–841 (2011).
30. C. Li et al., "Quantitative elastography provided by surface acoustic waves measured by phase-sensitive optical coherence tomography," *Opt. Lett.* **37**(4), 722–724 (2012).
31. B. F. Kennedy et al., "In vivo dynamic optical coherence elastography using a ring actuator," *Opt. Express* **17**(24), 21762–21772 (2009).
32. B. F. Kennedy et al.," In vivo three-dimensional optical coherence elastography, *Opt. Express* **19**(7), 6623–6634 (2011).
33. G. Y. Guan et al., "Depth profiling of photothermal compound concentrations using phase sensitive optical coherence tomography," *J. Biomed. Opt.* **16**(12), 126003 (2011).
34. J. B. Vorstius, "Modular bioreactor design for tissue engineering," Ph.D. Thesis, Mechanical Engineering, University of Dundee (2012).